Research Article

Serap Yiğit Gezgin, M. A. Basyooni-M. Kabatas*, Bedrettin Mercimek and Hamdi Şükür Kiliç

Effect of localized surface plasmon resonance of Au nanoparticles on the photovoltaic performance of CIGS/Si heterojunction structures

https://doi.org/10.1515/ntrev-2025-0290
Received November 19, 2025; accepted February 27, 2026;
published online April 21, 2026

Abstract: In this study, ultrathin $CuIn_xGa_{1-x}Se_2$ (CIGS) films with two distinct thicknesses were grown on n-Si substrates by pulsed laser deposition (PLD), with thickness controlled by varying the number of laser pulses. Au plasmonic nanoparticles were subsequently incorporated into the CIGS layers using the same PLD technique for photodetection applications. Owing to the localized surface plasmon resonance (LSPR) induced by the embedded Au nanoparticles, photon absorption within the CIGS layers was significantly enhanced across the visible and NIR spectral regions. Increasing the film thickness in the presence of Au nanoparticles promoted the formation of larger grains and yielded notable improvements in crystallinity. The dark electrical behavior of plasmonic and non-plasmonic *p*-CIGS/n-Si heterojunctions was analyzed using the conventional J–V method, as well as the Cheung–Cheung and Norde methods. Key diode parameters, including barrier height, ideality factor, and series resistance, were extracted and comparatively evaluated. Among the studied devices, the Au-CIGS2A heterojunction (based on Au-embedded CIGS thin film produced with 86,400 laser pulses) exhibited the most ideal diode characteristics, whereas the CIGS1A device (based CIGS thin film produced with 43,200 laser pulses) demonstrated the least favorable electrical performance. Under illumination, the combined effect of increased CIGS thickness and the LSPR-driven optical enhancement provided by the Au nanoparticles resulted in higher photovoltaic conversion efficiency in the corresponding heterojunction diodes.

Keywords: $CuIn_xGa_{1-x}Se_2$ (CIGS) ultrathin films; pulsed laser deposition; Au plasmonic nanoparticles; localized surface plasmon resonance; p-CIGS/n-Si heterojunction diodes

1 Introduction

Group I–III–VI_2 photovoltaic compounds, including $CuInSe_2$ (CIS) and $CuIn_xGa_{1-x}Se_2$ (CIGS), are pivotal semiconductor materials used as absorber layers in thin-film solar cell architectures. CIGS, a p-type absorber characterized by a high optical absorption coefficient, exhibits a tunable energy band gap ranging from approximately 1.0 to 1.7 eV and demonstrates excellent structural and chemical stability owing to its polycrystalline nature [1, 2]. The thickness of the CIGS thin film used as the absorber layer in thin-film solar cells typically ranges from 1 to 3 μm, ensuring adequate photon absorption and efficient charge-carrier generation within the device structure. In CIGS-based solar cells, the scarcity of indium (In) in the Earth's crust significantly contributes to the high production cost of devices employing CIGS absorber layers. To address this limitation, it is essential to minimize the consumption of indium-containing materials by reducing the absorber layer thickness while maintaining optimal photovoltaic conversion efficiency. CIGS or similar semiconductor layers fabricated with thicknesses below 500 nm are classified as ultrathin films [3]. The adoption of such ultrathin absorber structures has been demonstrated to enable substantial reductions in deposition time, energy consumption, and overall manufacturing costs, thereby enhancing the economic and practical feasibility of CIGS thin-film solar cell production.

***Corresponding author: M. A. Basyooni-M. Kabatas**, Department of Precision and Microsystems Engineering, Delft University of Technology, Mekelweg 2, 2628 CD Delft, Netherlands; Institute of Nanotechnology (INT), Karlsruhe Institute of Technology (KIT), Kaiserstraße 12, 76131 Karlsruhe, Germany; and Department of Nanotechnology and Advanced Materials, Graduate School of Applied and Natural Sciences, Selçuk University, 42030 Konya, Türkiye, E-mail: m.kabatas@tudelft.nl. https://orcid.org/0000-0001-8473-8253

Serap Yiğit Gezgin, Department of Physics, Faculty of Science, Selçuk University, 42031 Selçuklu, Konya, Türkiye

Bedrettin Mercimek, Chemistry Education Department, Ahmet Keleşoğlu Education Faculty, Necmettin Erbakan University, Konya, Türkiye. https://orcid.org/0000-0002-3407-6906

Hamdi Şükür Kiliç, Department of Metallurgical and Materials Engineering, Faculty of Engineering, Dokuz Eylül University, İzmir, Türkiye

Plasmonic metal nanoparticles, including Au, Ag, and Cu, have been extensively utilized as light-trapping components due to their remarkable optical phenomenon known as localized surface plasmon resonance (LSPR), which enables strong interaction with incident electromagnetic radiation and enhances optical absorption in photovoltaic and optoelectronic systems [4, 5]. When incident light interacts with a plasmonic nanoparticle, the conduction electrons within the nanoparticle become excited through the absorption of incident photons. These delocalized electrons collectively oscillate in resonance with the oscillating electromagnetic field of the incoming light; this phenomenon is referred to as LSPR [6]. Among plasmonic metals, gold exhibits outstanding resistance to chemical degradation and superior thermal endurance, ensuring prolonged functionality and stability when exposed to intense illumination or adverse environmental conditions [7, 8]. Au nanoparticles display an intense LSPR mode centered in the visible range of the electromagnetic spectrum [9]. The resonance wavelength can be systematically red-shifted into the near-infrared (NIR) region by controlling nanoparticle parameters such as areal density, aspect ratio, and vertical dimension [10, 11]. Incorporation of Au plasmonic nanoparticles into a semiconductor thin film promotes enhanced light absorption owing to the LSPR phenomenon. Additionally, plasmon decay facilitates the injection and formation of hot electrons inside the semiconductor. The resulting plasmonic semiconductor exhibits an elevated concentration of minority carriers, which contributes to a significant enhancement in photocurrent density and device conversion efficiency.

Zarerasouli et al. optimizes plasmonic Ag nanoparticles on the back surface of CIGS ultrathin solar cells, improving efficiency and current density, while exploring nanoparticle size, shape, and oxidation effects [12]. Londhe et al. demonstrates the enhancement of CIGS solar cells by depositing Au nanoparticles onto the CIGS layer, using dip coating and electrodeposition techniques [13]. In the studies of Zarerasouli and Bahador, it enhanced that CIGS ultrathin tandem solar cells by incorporating silver nanoparticle clusters, improving efficiency by 12.6 % through plasmonic light absorption enhancement [14]. Chen et al. work shows that plasmonic Au nanoparticles enhance CIGS flexible photovoltaics' efficiency by improving absorption, photocurrent, and carrier transport [15]. Zarerasouli et al. demonstrates that a cluster back reflector with cylindrical silver nanoparticles enhances J_{sc} and efficiency in CIGS ultrathin solar cells, achieving 27.2 mA/cm^2 and 15.7 % efficiency [16]. Park et al. represents that Au nanoparticles enhance CIGS solar cells by improving infrared absorption, reducing defect density, and increasing the band gap from 1.31 to 1.52 eV, boosting efficiency [17].

The preparation technique employed for nanoparticle fabrication is a key determinant of their morphological structure and uniformity. Pulsed laser deposition (PLD) provides remarkable flexibility and precision in nanoparticle fabrication, enabling the production of nanoparticles with specific morphological and optical properties. This technique enables fine control through multiple adjustable parameters, including substrate–target spacing, laser fluence, ambient gas pressure, and substrate temperature, throughout the deposition process [5, 18]. The PLD method enables fine-tuning of Au nanoparticle morphology, providing an effective means to control and tune the LSPR peak position across desired spectral regions, including both red- and blue-shifted wavelengths. In the PLD process, the number of laser pulses plays a critical role in tuning the plasmonic response; increasing the pulse number leads to a red shift of the LSPR peak, while decreasing it causes a blue shift toward shorter wavelengths [19].

This work reports the fabrication of plasmonic (Au nanoparticle-decorated) and non-plasmonic CIGS/n-Si heterojunction structures via the PLD method, in which Au plasmonic nanoparticles were embedded within a CIGS ultrathin absorber layer. Due to the LSPR property of Au nanoparticles, photovoltaic devices showed improvements driven by increased photoexcited electron-hole pair formation, hot-electron generation, and light scattering. In addition, doping with Au nanoparticles resulted in a greater improvement in photovoltaic performance than increasing the CIGS film thickness. CIGS/Si heterojunction photovoltaic devices offer somewhat lower efficiency values, but the LSPR effect of plasmonic Au nanoparticles provides opportunities to achieve higher efficiencies in such devices through easy fabrication without the need for more complex production techniques or the production of more layers. Under dark conditions, key parameters of the heterojunction devices, including barrier height (Φ_b), series resistance (R_s), and ideality factor (n), were extracted using conventional J–V, Norde, and Cheung–Cheung methodologies. The fill factor (FF), open-circuit voltage (V_{oc}), short-circuit current density (J_{sc}), and efficiency (η) of the fabricated heterojunction diodes were systematically evaluated. The effect of the LSPR of Au plasmonic nanoparticles on the photovoltaic performance of the heterojunction diode is examined in detail, and the main conclusions are drawn in this work.

2 Experimental

In this work, Ag/Au-CIGS/n-Si/Ag and Ag/CIGS/n-Si/Ag heterojunction diodes were fabricated. Au nanoparticles were deposited onto soda-lime glass (SLG) substrates at room

temperature using the PLD technique with a nanosecond laser (5 ns pulse width, 10 Hz repetition rate, 1,064 nm wavelength). The substrates were positioned 52 mm away from a high-purity Au target (99.95 %). Prior to deposition, the vacuum chamber was evacuated to a base pressure of 5×10^{-6} mbar using a rotary pump followed by a turbo-molecular pump. SLG substrates at room temperature (RT) were coated with Au nanoparticle thin films using 3,600, 5,400, 7,200, and 9,000 laser pulses at 0.5 J/cm^2 laser fluence (1,064 nm wavelength, 10 Hz repetition rate, and 5 ns pulse width). The experimental setup is schematically illustrated in Figure 1.

A CIGS target with 99.99 % purity was mounted on the target holder, and SLG and n-Si substrates were placed on the substrate holder. The vacuum inside the deposition chamber was first evacuated with a rotary pump and then further reduced to ~3×10^{-6} mbar using a turbo-molecular pump. The distance between the target and substrate was set to 45 mm. CIGS1 and CIGS2 thin-film layers were deposited onto the front (polished) surfaces of the n-Si wafers and SLG substrates at RT using 43,200 and 86,400 laser pulses with 0.25 J/cm^2 of laser fluency, respectively. The thickness of CIGS1 and CIGS2 thin films was determined as 75 nm and 180 nm, respectively, as seen in the Table in Figure 1. CIGS1 and CIGS2 thin films were embedded with Au nanoparticles by applying 7,200 laser pulses, as described in step 1, resulting in the formation of plasmonic Au-CIGS1 and Au-CIGS2 thin films, respectively. The back (matte) sides of the n-Si wafers were coated with Ag metal contacts by PLD. The CIGS thin film–coated SLG and n-Si wafers were subsequently vacuum-annealed at 450 °C for 5 min in a quartz tube furnace, as shown in Figure 1. Finally, Ag finger contacts were fabricated on the CIGS ultrathin films by physical vapor deposition (PVD). The completed configurations of the non-plasmonic CIGS1&CIGS2/n-Si (CIGS1A and CIGS2A) and plasmonic Au-CIGS1&Au-CIGS2/n-Si heterojunction diodes (Au-CIGS1A and Au-CIGS2A) are illustrated in Figure 1, respectively.

The surface morphology, topography, stoichiometric composition, crystalline ordering, and optical transmittance

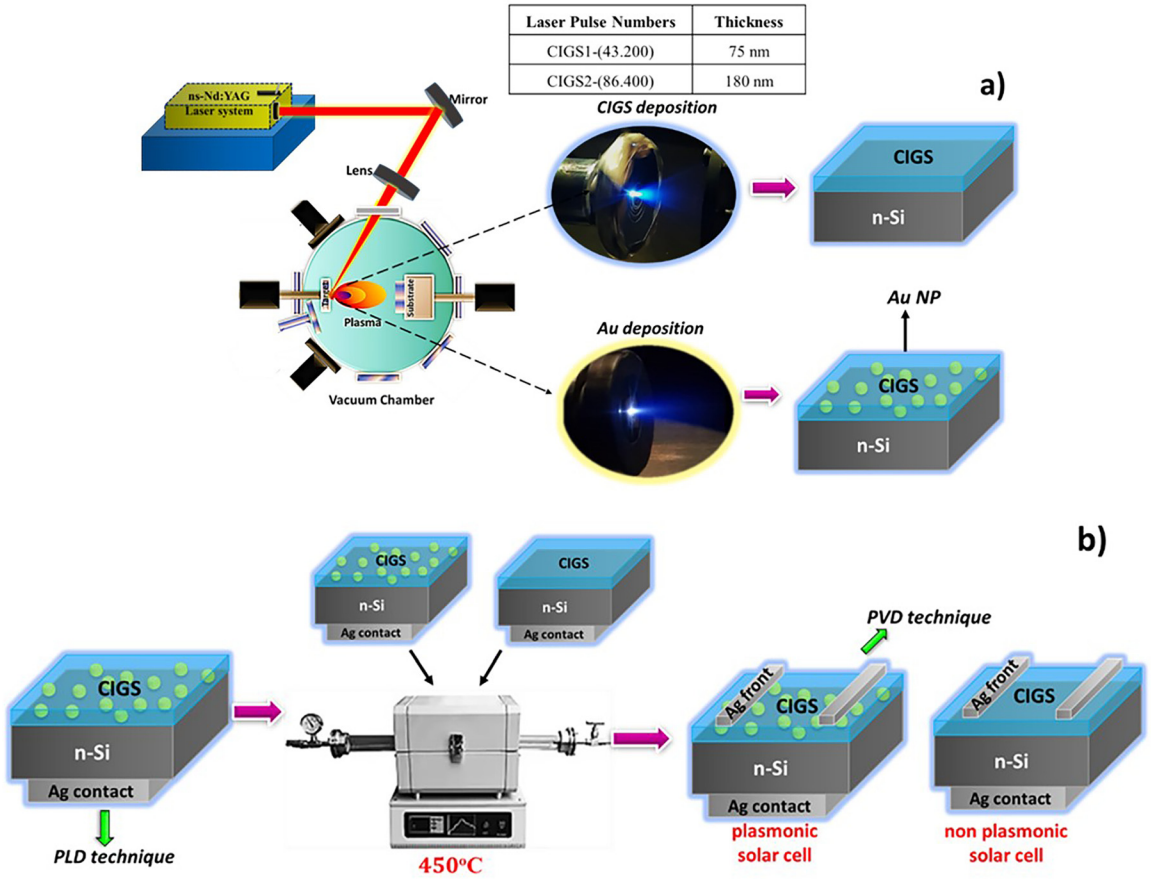

Figure 1: Thin film deposition process. (a) Schematic illustration of the fabrication steps of plasmonic (Au nanoparticle–embedded) and non-plasmonic CIGS/n-Si heterojunction solar cells: Deposition of CIGS ultrathin films on n-Si by ns-Nd: YAG-based PLD, incorporation of Au nanoparticles into the CIGS layer, b) Ag back-contact formation, post-annealing at 450 °C in a quartz tube furnace, and final Ag front-contact patterning.

of the non-plasmonic and plasmonic CIGS ultrathin films were analyzed using atomic force microscopy (AFM), scanning electron microscopy with energy-dispersive X-ray spectroscopy (SEM–EDX), X-ray diffraction (XRD) (working parameters are that scan rate is 2°/min and step size is 0.02°), and UV–Vis spectroscopy, respectively. The optical properties of CIGS thin films were measured relative to a baseline of SLG, ensuring precise calibration and consistency for comparative analysis of their optical behavior. The current–voltage (J–V) characteristics of both device types (CIGS/n-Si heterojunctions) were recorded in the dark and under AM1.5 illumination (80 mW/cm^2). For J-V measurements, an Ag thin-film metal contact was employed for the front electrode, while an Ag thin-film contact was utilized for the rear electrode.

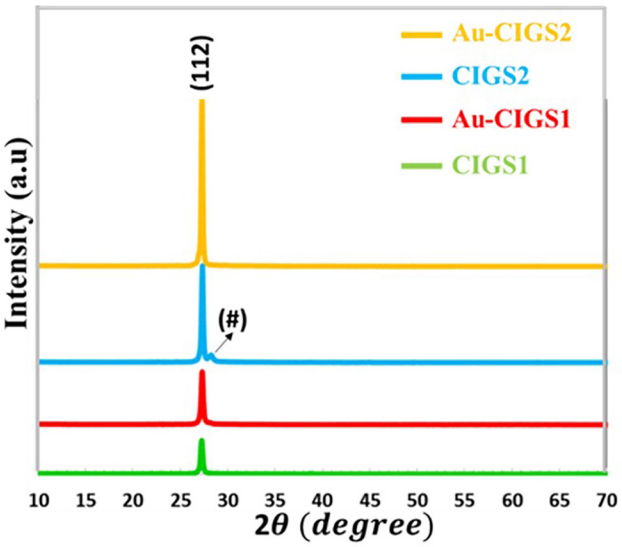

Figure 2: X-ray diffraction (XRD) patterns of non-plasmonic CIGS1 and CIGS2 ultrathin films and plasmonic Au-CIGS1 and Au-CIGS2 ultrathin films deposited by PLD with 43,200 and 86,400 laser pulses, respectively.

3 Results and discussion

3.1 XRD property

Figure 2 presents the X-ray diffraction (XRD) patterns of CIGS1 and CIGS2 ultrathin films deposited using 43,200 and 86,400 laser pulses, together with the corresponding plasmonic Au-CIGS1 and Au-CIGS2 thin films, in which Au atoms were incorporated into the CIGS ultrathin layers by 7,200 laser pulses. The XRD patterns in Figure 2 indicate that all CIGS ultrathin films are monocrystalline with a strong preferred orientation along the (112) plane, exhibiting a dominant diffraction peak at 2θ ≈ 27.3° [20–22]. A progressive increase in the number of laser pulses leads to a corresponding increase in the (112) diffraction peak intensity, indicating improved crystallinity [23]. The incident CIGS species more effectively occupy energetically favorable atomic sites on the substrate surface, resulting in more uniform nucleation and enhanced crystalline ordering within the CIGS ultrathin films. A second phase (#), appearing as a small shoulder on CIGS2 ultrathin film, was observed at 2θ = 28.21°. The distribution of Ga atoms within the CIGS2 ultrathin film is non-uniform, with limited diffusion characteristics. As a result, the Ga-rich phase that forms within the film can be attributed to the presence of this secondary phase. Furthermore, crystallization along the (112) direction in the CIGS ultrathin films is notably strengthened as a consequence of Au nanoparticle incorporation [24].

The average crystallite size of the thin films was calculated using the Scherrer eq [23].:

$$S = 0.94\lambda/\beta \cos\theta \quad (1)$$

where S is the average crystallite size, β is the full width at half maximum (FWHM) of the main diffraction peak, θ is the Bragg angle, and λ\lambdaλ is the wavelength of the X-ray beam used. According to this analysis, the crystallite sizes of the CIGS1, Au-CIGS1, CIGS2, and Au-CIGS2 thin films were found to be 32.47 nm, 35.15 nm, 43.14 nm, and 49.66 nm, respectively. With increasing film thickness, the grains constituting the CIGS ultrathin films exhibit noticeable growth. The CIGS1 ultrathin film, characterized by its smaller thickness, contains smaller grains and consequently a higher density of structural imperfections, which deteriorates its crystallinity. As the grain size increases in the CIGS2 ultrathin films, the grain boundary density decreases, and defect states are partially passivated, resulting in enhanced crystalline order and improved structural quality [25–28]. So, the increase in film thickness accelerates nucleation, promoting the aggregation of more atoms. As additional nuclei form, they coalesce, enhancing grain size. As the film thickness increases, more surface area is available for diffusion, allowing atoms to move inward from the crystalline surfaces. Thicker films facilitate greater atomic mobility, thereby enhancing diffusion. This atomic movement leads to the growth of larger crystals or grains.

In addition, incorporating Au nanoparticles further increases the crystallite size compared with non-plasmonic CIGS thin films [24, 29]. The presence of Au nanoparticles may enhance the intensity of the main diffraction peak, which may be attributed to the substitutional occupation of Se^{4+} vacancies (64 pm) by Au^{+1} ions (151 pm) [30]. This atomic incorporation may facilitate grain growth and improve the overall crystalline quality of the thin films. Furthermore, large Au^{+1} ions have larger radii and therefore lower bond

Table 1: The crystalline size, dislocation density, and micro-strain parameters of plasmonic and non-plasmonic CIGS ultrathin films.

Samples	Crystalline size (nm)	Dislocation density $\times 10^{14}$ (lines/m^2)	Micro-strain $\times 10^{-3}$
CIGS1	32.47	9.48	1.11
Au-CIGS1	35.15	8.09	1.03
CIGS2	43.14	5.37	0.83
Au-CIGS2	49.66	4.05	0.72

energies. This may lead to a more flexible lattice, as the bonds between large ions are weaker than those between small ions. In this case, the lattice may expand more easily (Table 1).

Dislocation density (δ) and microstrain (ε), quantifying defect concentrations that adversely affect the crystallographic quality of the thin films, are computed using eq. (2) and eq. (3) [23]:

$$\delta = 1/D^2 \tag{2}$$

$$\varepsilon = \beta \cos\theta/4 \tag{3}$$

Dislocation density quantifies the total length of dislocation lines per unit volume, or equivalently, the number of dislocations per unit area, in a crystalline solid. Microstrain refers to local variations in interplanar spacing resulting from defects, internal stresses, or lattice distortions within the crystal lattice. Embedding Au nanoparticles into the CIGS ultrathin films leads to a modest reduction in structural defects and trap states, which in turn decreases both the dislocation density and the microstrain [31–33].

3.2 Surface characterization

According to the SEM images shown in Figure 3, an increase in the number of laser pulses results in a corresponding enlargement of the particle size. This behavior can be attributed to the higher density of atoms deposited laterally and vertically with increasing pulse number, which promotes particle coalescence and the formation of larger agglomerated clusters [34, 35]. The thicknesses of the thin films deposited using 43.200 and 86.400 laser pulses were determined to be 75 nm and 180 nm, respectively. The average particle size of CIGS1, CIGS2, Au-CIGS1, and Au-CIGS2 thin films is 40.72 nm, 57.72 nm, 58.65 nm, and 74. 38 nm according to the small square on the SEM images in Figure 3. In addition, incorporation of Au atoms into the CIGS nanoparticles results in a further increase in particle size, as Au atoms occupy suitable vacant sites within the CIGS structure and promote particle growth through atomic filling and structural densification. The resulting reduction in the number of grain boundaries within the thin films facilitates the passivation of defect states and electronic traps at intergranular regions, thereby enhancing crystalline ordering, reducing non-radiative recombination centers, and improving the structural integrity of the films.

Based on the elemental ratios presented in Table 2 and the SEM–EDX spectra shown in Figure 4, the CIGS ultrathin films exhibit a Cu-deficient and In-rich composition. During the growth of the CIGS1 ultrathin film, the relatively low deposition rate leads to a noticeable deviation from stoichiometric transfer, resulting in pronounced Cu deficiency and In enrichment. The excessive indium atoms tend to occupy copper vacancy sites (V_{Cu}), forming In_{Cu} antisite donor defects [36, 37]. These donor-type defects act as recombination centers, thereby degrading charge-carrier transport and adversely affecting the photovoltaic performance of the CIGS device. As ultrathin film thickness increases, the stoichiometric transfer progressively approaches the ideal CIGS composition, primarily due to the enhanced deposition rate. This improvement results in an increase in Cu concentration and a concurrent decrease in In content. Consequently, the formation of In_{Cu} donor defects is significantly suppressed, reducing defect-induced recombination centers and improving the optoelectronic quality of the film. A decrease in the Se concentration is also observed in the CIGS ultrathin films, which can be attributed to partial substitution of Se anions or occupation of Se-related vacancies by Au ions during the incorporation process [38–40].

The AFM images shown in Figure 5 display the three-dimensional (3D) and two-dimensional (2D) surface topographies of the plasmonic and non-plasmonic CIGS ultrathin films, providing detailed information on their morphological features and surface roughness distributions. The 2D AFM images exhibit a strong correlation with the corresponding SEM micrographs, indicating good consistency between the surface morphology observed by AFM and the structural features revealed by SEM. AFM observations confirm that increasing the number of laser pulses, together with the incorporation of Au nanoparticles into the CIGS ultrathin films, promotes particle growth. This behavior can be attributed to enhanced surface-atom mobility and localized coalescence processes induced by Au incorporation, leading to the formation of larger grains and an overall increase in surface roughness and structural compactness.

The root-mean-square surface roughness values of the CIGS1, Au-CIGS1, CIGS2, and Au-CIGS2 ultrathin films were determined to be 13.32 nm, 19.89 nm, 28.34 nm, and 37.71 nm, respectively, indicating a systematic evolution of the surface morphology with changes in film growth conditions. The

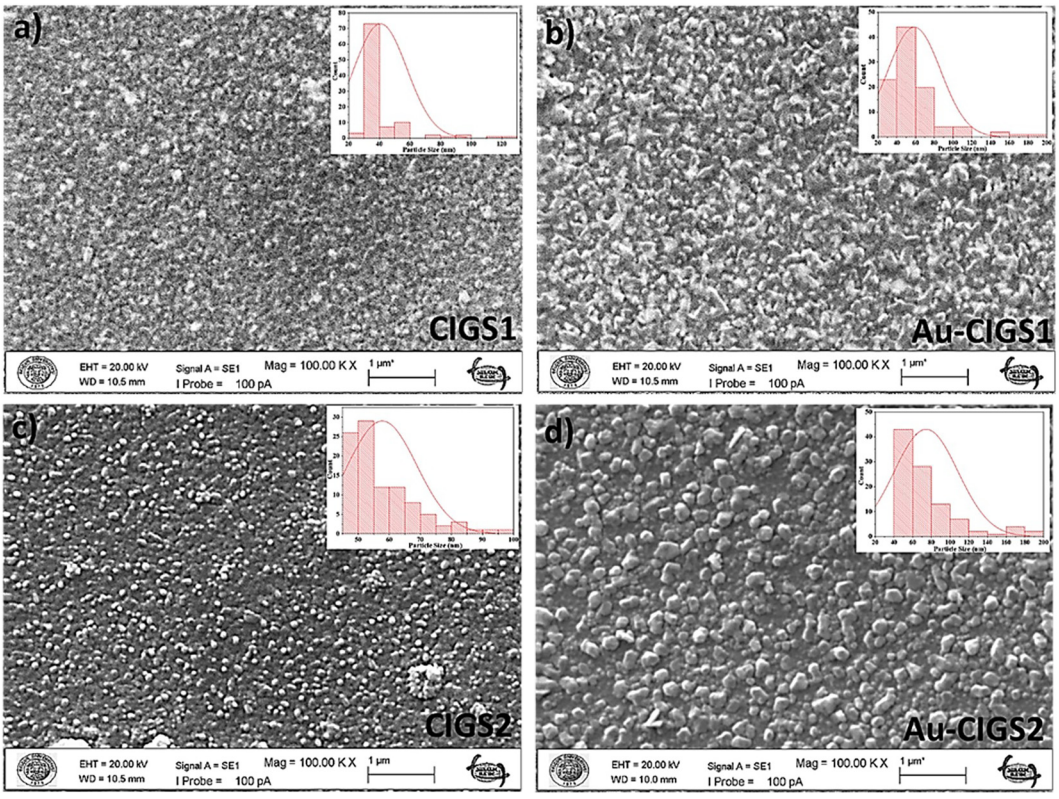

Figure 3: SEM images of a) CIGS1, b) Au-CIGS1, c) CIGS2, and d) Au-CIGS2 ultrathin films.

Table 2: The atomic weight rates of elements in CIGS1, Au-CIGS1, CIGS2 and Au-CIGS2 ultrathin films.

Ultrathin films	Au (%)	Cu (%)	In (%)	Ga (%)	Se (%)
CIGS1	–	16.67	27.65	4.59	51.09
Au-CIGS1	6.41	15.93	28.48	5.27	43.91
CIGS2	–	19.78	21.80	6.06	52.36
Au-CIGS2	5.75	20.38	22.12	6.31	45.44

increase in particle size results in a corresponding rise in surface roughness, indicating that the growth and coalescence of larger grains contribute to the enhanced surface irregularities in the thin films.

3.3 The optical properties

3.3.1 Localized surface plasmon resonance (LSPR) of Au nanoparticles

According to the absorption spectra shown in Figure 6, Au nanoparticles synthesized on soda–lime glass using laser irradiation with 3.600, 5.400, 7.200, and 9.000 pulses exhibit LSPR peaks located at approximately 564 nm, 620 nm, 712 nm, and 772 nm, respectively. The observed redshift of the resonance wavelength with increasing laser pulse number indicates systematic nanoparticle growth and enhanced plasmonic coupling among adjacent particles. This behavior can be explained as follows: when the electromagnetic field of the incident light interacts with the conduction electrons in the nanoparticles, it induces charge separation, thereby forming an oscillating electric dipole. The Coulombic restoring force drives these electrons to oscillate at a specific resonance frequency [10, 11, 41, 42]. As nanoparticle size increases, phase retardation reduces the restoring force, lowering the resonance energy and redshifting the LSPR peak toward longer wavelengths. According to the particle size distributions seen in the small squares in the SEM images in Figure 6, when the laser pulse number increased from 3.600 to 9.000, the average particle size of the deposited Au nanoparticles increased from 34.99 nm to 65.36 nm. LSPR bandwidth increases, and the peak position redshifts as the particle size increases. Moreover, once the Au nanoparticle diameter exceeds approximately 80 nm, electron oscillations generate photon emission via light scattering, leading to radiation

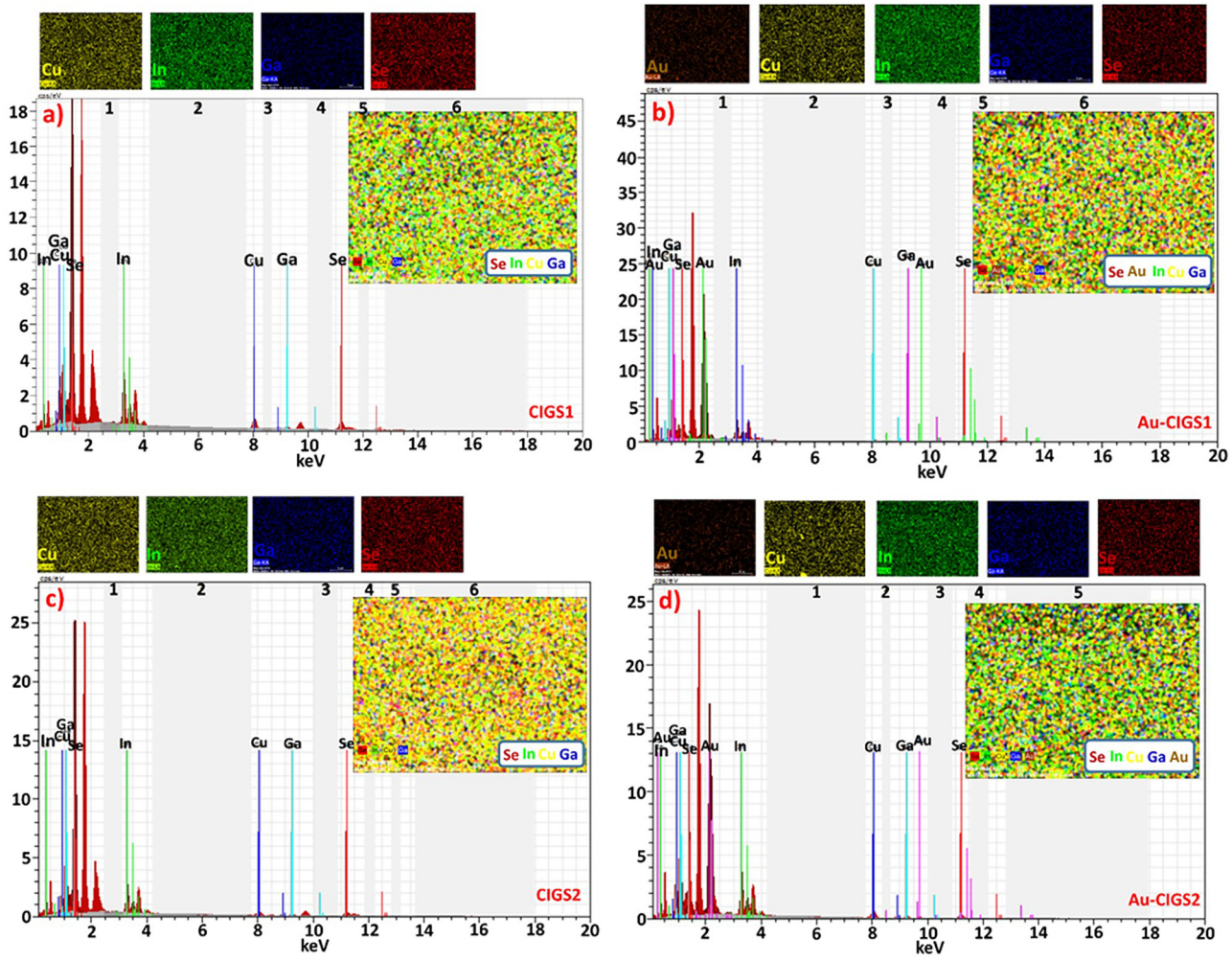

Figure 4: SEM-EDX spectrums of a) CIGS1, b) Au-CIGS1, c) CIGS2 and d) Au-CIGS2 ultrathin films.

damping. This effect further lowers the oscillation frequency and energy, disrupts phase coherence, and produces an additional redshift of the LSPR peak, as indicated by the normalized absorbance spectrum in Figure 6 [43].

Near-field coupling between Au nanoparticles also plays a crucial role in shifting the LSPR peak toward the NIR region. As illustrated in Figure 6, increasing the laser pulse number from 3,600 to 9,000 results in a higher surface density of deposited Au nanoparticles, thereby reducing interparticle spacing and enhancing near-field interactions. When the polarization of the incident light is aligned with the interparticle axis, the induced dipoles generate localized electric fields around neighboring particles. The mutual electromagnetic coupling among adjacent Au nanoparticles leads to strong local field enhancement and a further redshift of the LSPR peak toward longer wavelengths [10, 11, 41, 44, 45].

3.3.2 Optical response of plasmonic and non-plasmonic CIGS ultrathin films

According to the absorption spectra shown in Figure 7a, the CIGS2 ultrathin film exhibits higher photon absorption in both the UV and visible regions than the CIGS1 film. This enhancement can be attributed to the larger grain size and higher particle density of the CIGS2 film, which increase the effective optical path length and the surface area available for photon interaction, thereby promoting more efficient light absorption within the film. As seen in Figure 7b and c, the plasmonic CIGS1 and CIGS2 ultrathin films display a pronounced absorption peak in the visible region and an overall enhancement of absorption extending into the near-infrared (NIR) region due to the LSPR of the embedded Au nanoparticles. This plasmon-induced enhancement arises from the collective oscillation of conduction electrons in the

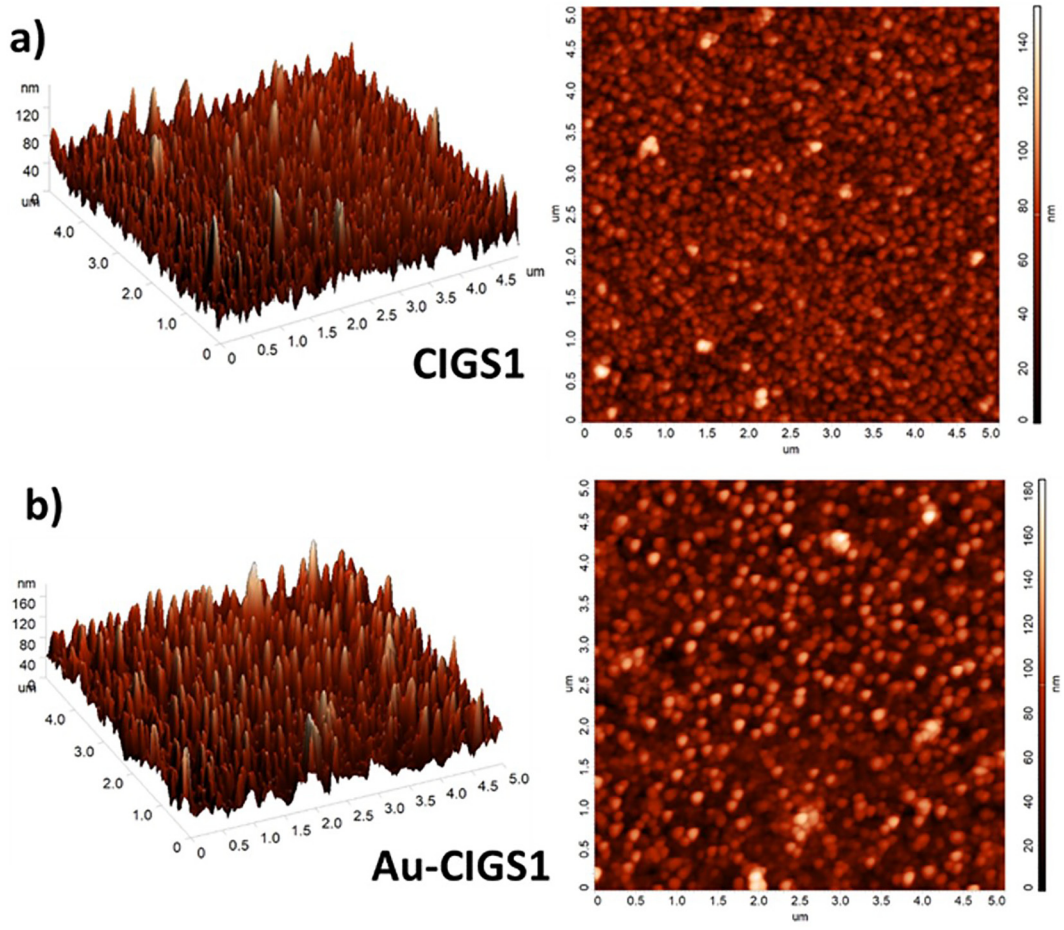

Figure 5: 3D and 2D (5 × 5 area) images of a) CIGS1, b) Au-CIGS1, c) CIGS2 and d) Au-CIGS2 ultrathin films.

Au nanoparticles, which amplifies the local electromagnetic field and strengthens light–matter interaction in the CIGS ultrathin films.

The optical band-gap values of the films were determined using the Tauc relation [46], which relates the absorption coefficient α to the photon energy hν for direct allowed transitions:

$$\alpha h\nu = A\left(h\nu - E_g\right)^{1/2} \tag{4}$$

where A is a constant and $E_g$is the optical band-gap energy. The band-gap energy was obtained from the Tauc plots shown in Figure 7d by extrapolating the linear portion of $(\alpha h\nu)^2$ versus (hν) versus hνh\nuhν curves to the photon-energy axis, where the absorption coefficient tends to zero. Using this procedure, the band gaps of the CIGS1, CIGS2, Au-CIGS1, and Au-CIGS2 ultrathin films were determined to be 2.92 eV, 2.20 eV, 1.80 eV, and 1.44 eV, respectively. The difference between CIGS1 and CIGS2 indicates that changes in thickness and microstructure affect the optical transition energy. In the very thin CIGS1 thin film, carriers (electrons or holes) move within a confined region, which can lead to energy-level separation and a broadening of the band gap. Shallow defects near the surface create new energy levels within the band gap. These levels provide new pathways for carriers (electrons or holes) to traverse, thereby narrowing the band gap of the CIGS2 thin film. Incorporation of Au plasmonic nanoparticles further modifies the absorption edge and leads to a blue shift of the apparent optical band gap, reflecting the combined influence of LSPR-induced field enhancement, changes in defect distribution, and possible compositional or structural variations within the CIGS ultrathin films [9, 47, 48].

The absorption coefficient (α) of thin films is expressed by $\alpha = 2.303*\left(\frac{A}{T}\right)$ equation, where A represents absorbance and T indicates film thickness. According to the graphs 7e and 7f, in the visible and NIR wavelength range, the CIGS1 thin film has an absorption coefficient in the range of 1.3–$3 \times 10^{+4}$ cm-1, while the Au-CIGS1 thin film shows an absorption coefficient of 4.5–5.7 × 10 + 4 cm-1 in this wavelength range. CIGS-2 thin film exhibited α value in the range

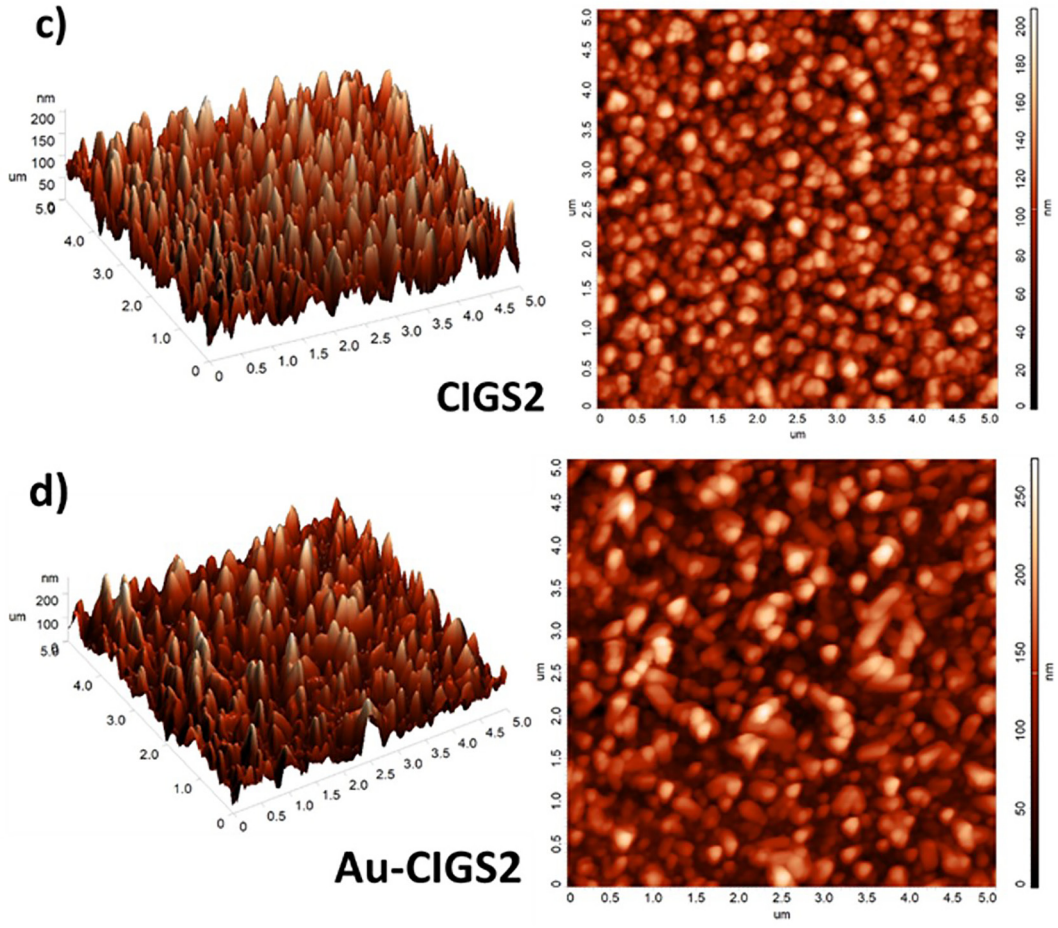

Figure 5: Continued.

of $5.5 \times 10^{+3}$ cm^{-1} to $2 \times 10^{+4}$ cm^{-1} at visible-NIR wavelength. With the embedding of Au nanoparticles, the Au-CIGS2 thin film has an α value of approximately $2.6–3.3 \times 10^{+4}$ cm^{-1}. This shows that embedding Au plasmonic nanoparticles into CIGS thin films results in these films absorbing more photons, particularly in the visible and NIR regions.

3.4 Electrical properties of non-plasmonic and plasmonic CIGS/n-Si heterojunction diodes in the dark

The diode current density can be described by the thermionic emission (TE) model, which relates the current density across the junction to the thermally activated transport of charge carriers over the potential barrier at the interface [49].

$$J = J_0\left[\exp\left(\mathrm{qV}/\mathrm{nkT}\right) - 1\right] \tag{5}$$

Here, V is the applied forward-bias voltage, J_0 is the reverse saturation current density, k is the Boltzmann constant, n is the diode ideality factor, q is the elementary charge, and T is the absolute temperature. The ideality factor, which provides information on the dominant carrier-transport mechanism and the deviation from ideal TE behavior, was calculated from [50, 51]:

$$n = \frac{q}{\mathrm{kT}}\frac{\mathrm{dV}}{d\left(\ln \mathrm{J}\right)} \tag{6}$$

where J denotes the forward-bias current density. The ideality factor was extracted from the linear region of the forward-bias part of the logarithmic J–V characteristics, as shown in Figure 8 (in the small square). The slope of this region reflects the exponential dependence of the current density on the applied voltage, providing insight into carrier transport and recombination processes in the diode.

The relatively low crystallinity and small grain size of the CIGS1 ultrathin film favor carrier trapping at grain boundaries, thereby reducing carrier lifetime and limiting

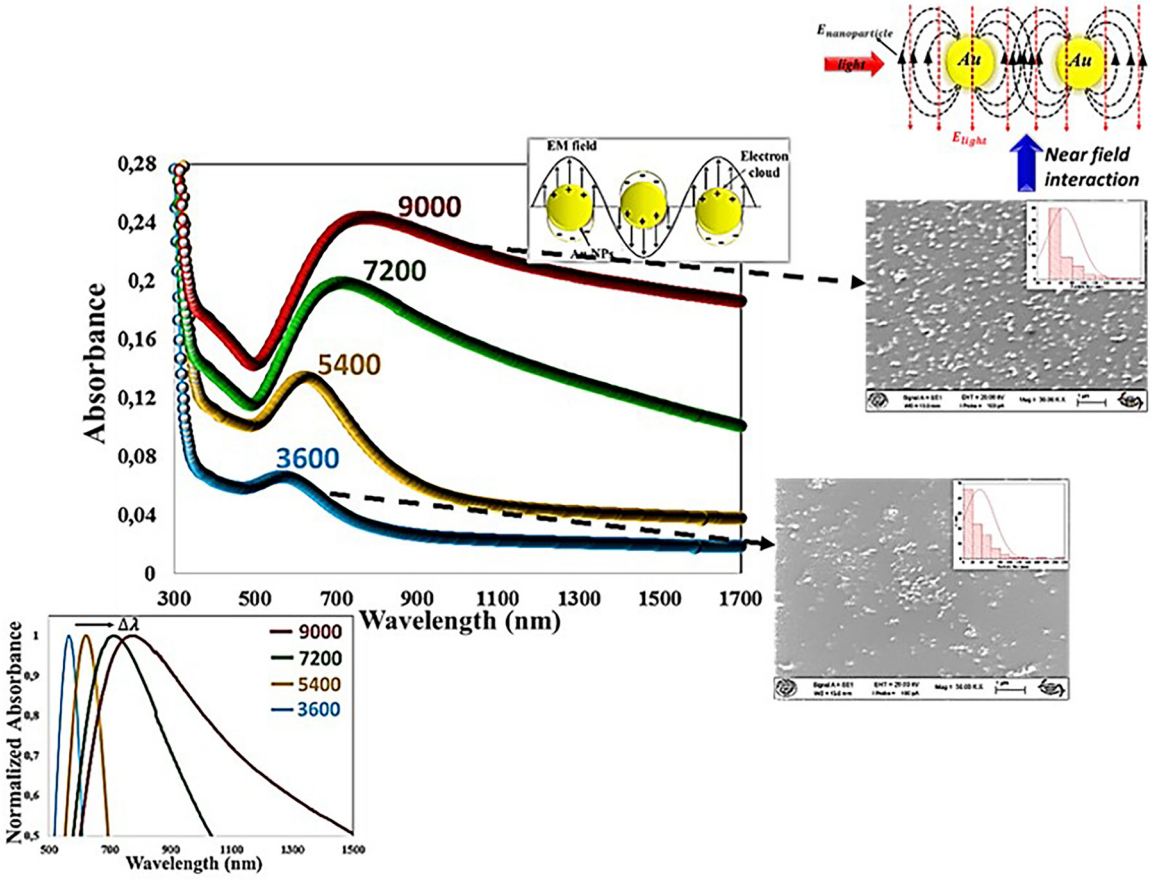

Figure 6: Optical absorption characteristics of Au nanoparticles grown on SLG with 3,600, 5,400, 7,200, and 9,000 laser pulse numbers.

charge transport through the absorber layer. In addition, less favorable band alignment between the CIGS1 layer and the n-Si substrate can further hinder efficient carrier transfer across the heterojunction interface [52, 53]. These structural and electronic limitations collectively contribute to the higher ideality factor observed in the CIGS1A heterojunction diode (Table 3). Increasing the film thickness and incorporating Au nanoparticles can enhance crystallinity, promote grain growth, and facilitate the passivation of trap states at grain boundaries, thereby extending the carrier lifetime. These modifications, together with the associated changes in band alignment between the two semiconductor layers, are expected to reduce the ideality factor and enhance the overall performance of the diodes [24, 54].

The barrier height (Φ_b) of the diode was determined using eq. (7), which relates the potential energy barrier at the metal–semiconductor interface to the diode's electrical characteristics, providing insight into charge carrier transport across the junction.

$$\Phi_b = \frac{\mathrm{kT}}{q}\ln\left(\frac{\mathrm{AA}^* T^2}{J_o}\right) \tag{7}$$

where A is the diode active area, and A^* is the effective Richardson constant (112 A cm^{-2} K^{-2} for n-type Si). The reverse saturation current density J_0 was obtained from the intercept of the linear fit to the dark logarithmic J–V characteristics, as illustrated in Figure 8 (in the small square). Variations in absorber-layer microstructure and composition lead to differences in the built-in potential across the depletion region and, consequently, in the effective Schottky barrier height at the CIGS/n-Si interface (Table 3). Devices based on thinner, more defective absorbers exhibit a higher effective barrier and poorer charge transport, whereas those with thicker and structurally improved absorbers show a reduced barrier height and enhanced carrier transport across the junction.

The series resistance (R_{series}) [55] of heterojunction diodes is evaluated using eq. (8):

$$R_{\mathrm{series}} = \frac{\Delta V_{\mathrm{forward\ bias\ voltage}}}{\Delta I_{\mathrm{forward\ bias\ current\ density}}} \tag{8}$$

where $\Delta V_{\mathrm{forward}}$ and $\Delta J_{\mathrm{forward}}$ denote the changes in forward-bias voltage and current density, respectively. The series resistance was obtained from the ratio of the voltage

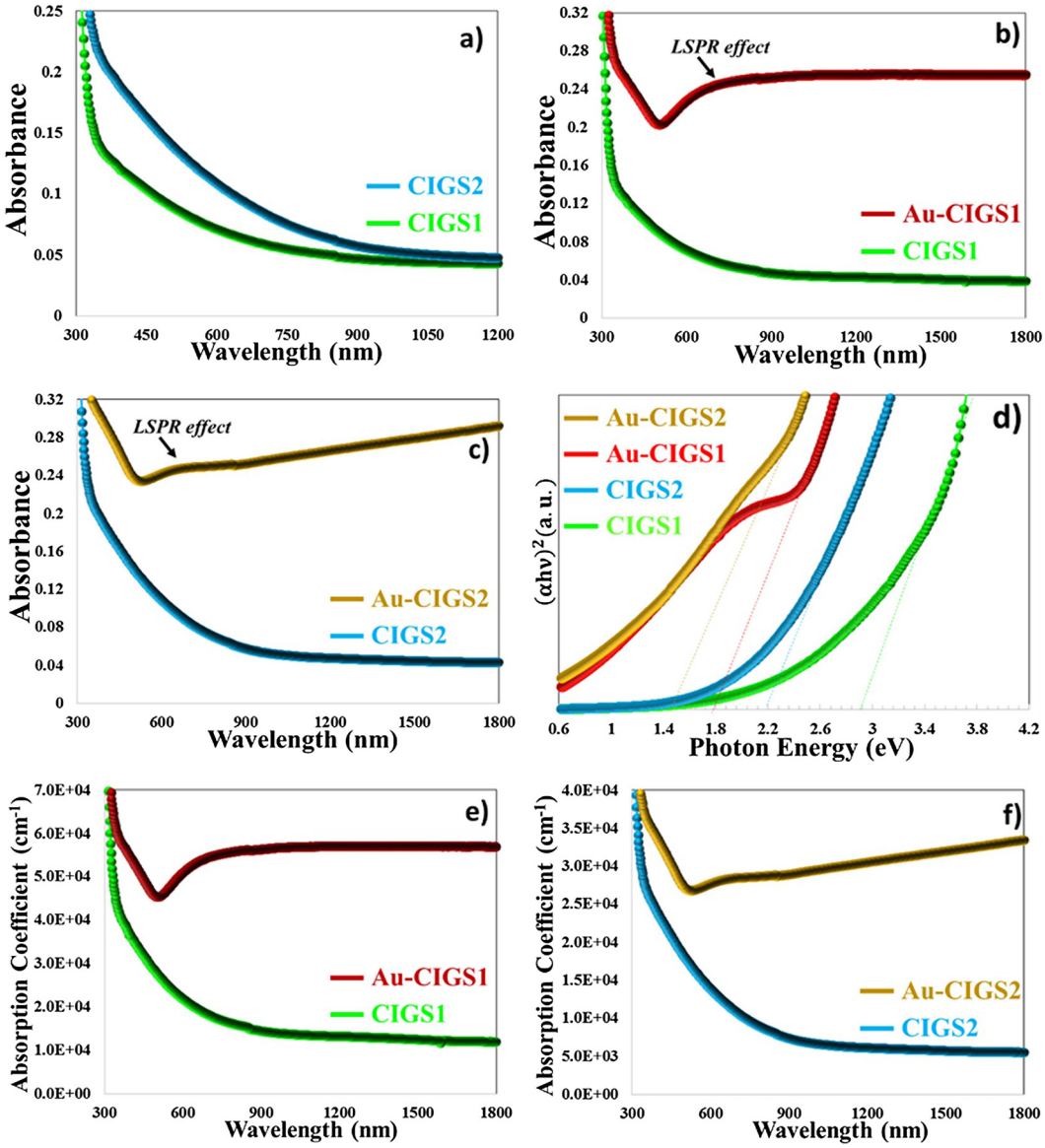

Figure 7: Optical properties. (a, b, c) The absorption spectra and (d) Tauc plots of the non-plasmonic and plasmonic CIGS ultrathin films, (e-f) the absorption coefficient.

variation to the corresponding current density variation in the forward-bias region. This resistance plays a crucial role in determining the electrical behavior and efficiency of the solar cell by influencing carrier transport, voltage drop, and power conversion efficiency. In particular, (R_{series}), quantifies resistive losses within the device and reflects the combined effects of contact resistance and semiconductor-layer bulk resistance on the diode's overall electrical performance.

The high series resistance observed in the CIGS1-A diode (Table 3 and Figure 9) may be attributed to several factors, including the poor crystallinity of the CIGS ultrathin film, which results in a low carrier concentration; a relatively high surface resistance; and interfacial issues such as oxide-layer formation, contamination, surface roughness, or diffusion-induced interlayers at the junction interface. These factors collectively hinder efficient charge transport and lead to increased series resistance within the device [56, 57]. Increasing the absorber-layer thickness and incorporating Au plasmonic nanoparticles enhances the crystallinity and crystal quality of the CIGS films, thereby increasing the carrier concentration within the material. As a result, the overall film resistance decreases, reducing the series resistance of the corresponding diodes.

The values of n, R_s and Φ_b for the heterojunction structures can also be extracted using the Cheung–Cheung

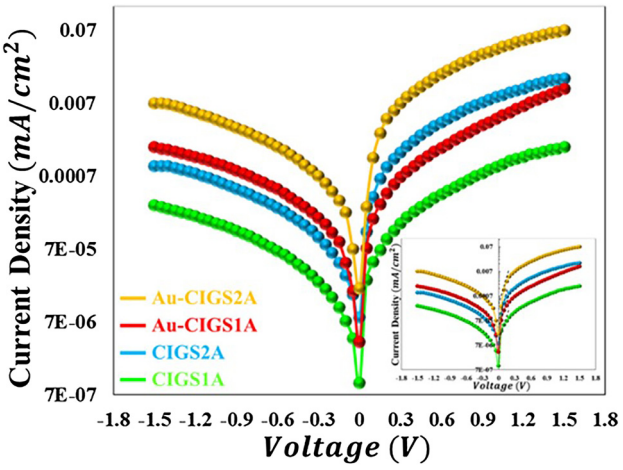

Figure 8: Logarithmic J–V characteristics of non-plasmonic and plasmonic CIGS/n-Si heterojunction diodes measured in the dark, under a bias voltage range of –1.5 V to +1.5 V, at room temperature.

method [58]. The analytical framework of the Cheung–Cheung approach is expressed through eqs. (9)–(11), which provide a systematic means of determining these parameters from the forward bias region of the (*J-V*) characteristics:

$$\frac{\mathrm{dV}}{\mathrm{d}(\ln \mathrm{J})} = \mathrm{JR}_s + n\left(\frac{\mathrm{kT}}{q}\right) \tag{9}$$

$$H(J) = V - \left(\frac{\mathrm{nkT}}{q}\right)\ln\left(\frac{J}{\mathrm{AA}^{*}T^{2}}\right) \tag{10}$$

$$H(J) = \mathrm{JR}_s + n\Phi_b \tag{11}$$

dV/dln(*J*)-*J* characteristics of the heterojunction are presented in Figure 10, which were derived based on eq. (10). The slope and the *y*-intercept of the dV/dln(*J*)-*J* plots correspond to R_s and nkT/*q*, respectively. Meanwhile, H(*J*)-*J* characteristics displayed in Figure 10 were obtained from the forward-bias region of the logarithmic *J-V* characteristics shown in Figure 10, as determined using Eq. (11). According to Eq. (12), the slope and *y*-intercept of the H(*J*)-*J* plot representJR_s and $n\Phi_b$, respectively. The (R_{series}) values of CIGS/n-Si heterojunctions obtained through both the conventional *J-V* analysis and the Cheung–Cheung approach were found to be in close agreement, whereas the barrier height values derived from the Cheung–Cheung method were observed to be slightly lower than those determined by the conventional *J-V* technique, as presented in Table 3. This discrepancy can be attributed to the fact that, while the conventional *J-V* analysis considers the reverse bias region, and the Cheung–Cheung method evaluates the high-voltage region under forward bias conditions. The relatively higher ideality factor obtained from the Cheung–Cheung method can be attributed to the evaluation being performed in the high-voltage (nonlinear) forward-bias region, whereas the conventional J–V method determines this parameter in the lower-voltage region.

F(*V*)–*V* characteristics of heterojunctions under dark conditions are illustrated in Figure 11a. The barrier height and series resistance, which were evaluated using the Norde method, as defined by eqs. (12)–(14) [59].

$$F(V,\gamma) = \frac{V}{\gamma} - \frac{\mathrm{kT}}{q}\ln\left(\frac{J(V)}{\mathrm{AA}^{*}T^{2}}\right) \tag{12}$$

where γ represents the first constant value greater than the ideality factor, which is obtained from the log. *J-V* characteristics.

$$\Phi_b = F(V_o) + \frac{V_o}{\gamma} - \frac{\mathrm{kT}}{q} \tag{13}$$

$$R_s = \frac{\gamma - n}{I_{\min}}\frac{\mathrm{kT}}{q} \tag{14}$$

$F(V_o)$ parameter corresponds to the minimum point of the *F*(*V*)–*V* plot, with V_o being the voltage at which this minimum occurs, and $I_{\min}$ representing the current density value corresponding to V_o in the *J-V* characteristics As shown in Table 3, R_s and Φ_B parameters obtained from the Cheung–Cheung and

Table 3: Electrical parameters of non-plasmonic and plasmonic CIGS/n-Si heterojunctions (CIGS1A, CIGS2A, Au-CIGS1A, Au-CIGS2A) calculated from J–V characteristics using the conventional, Cheung–Cheung, and Norde methods under dark conditions.

Samples	The conventional			Cheung Cheung				Norde	
	J-V			dV/dln(*J*)-*J*		*H*(*J*)-*J*		*F*(*V*)	
	n	ϕ_b (eV)	R_s (Ω.cm^2)	*n*	R_s (Ω.cm^2)	ϕ_b (eV)	R_s (Ω.cm^2)	ϕ_b (eV)	R_s (Ω.cm^2)
CIGS1A	5.02	0.71	455.49	8.11	359	0.62	415.67	0.62	266
CIGS2-A	3.51	0.67	68.08	5.79	51.81	0.56	59.29	0.57	19.5
Au-CIGS1A	3.65	0.64	56.40	8.88	40.23	0.58	53.85	0.59	50.6
Au-CIGS2A	1.66	0.61	15.12	5.41	11.86	0.52	13.64	0.57	7.02

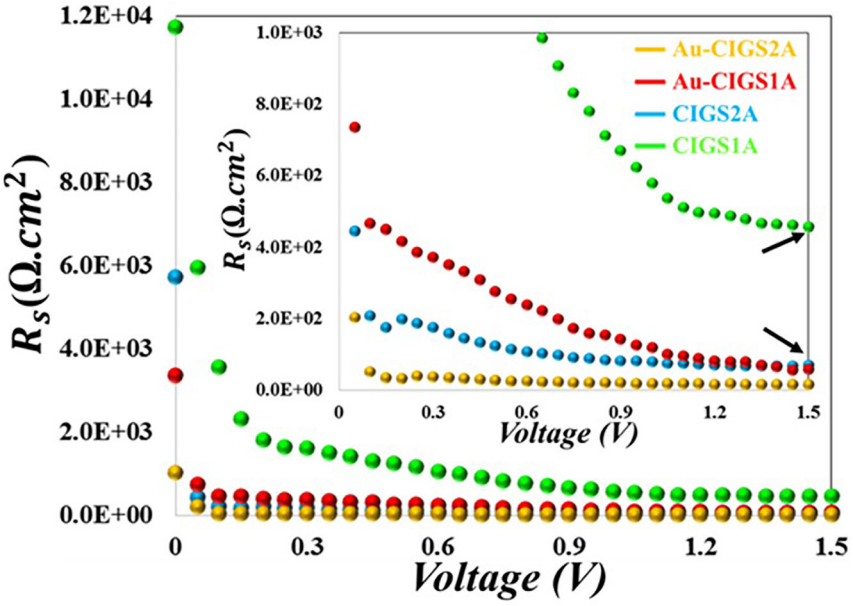

Figure 9: Series resistance (R_s) as a function of applied voltage for plasmonic and non-plasmonic CIGS/n-Si heterojunctions measured in the dark under a bias voltage range of +1.5 V, at room temperature.

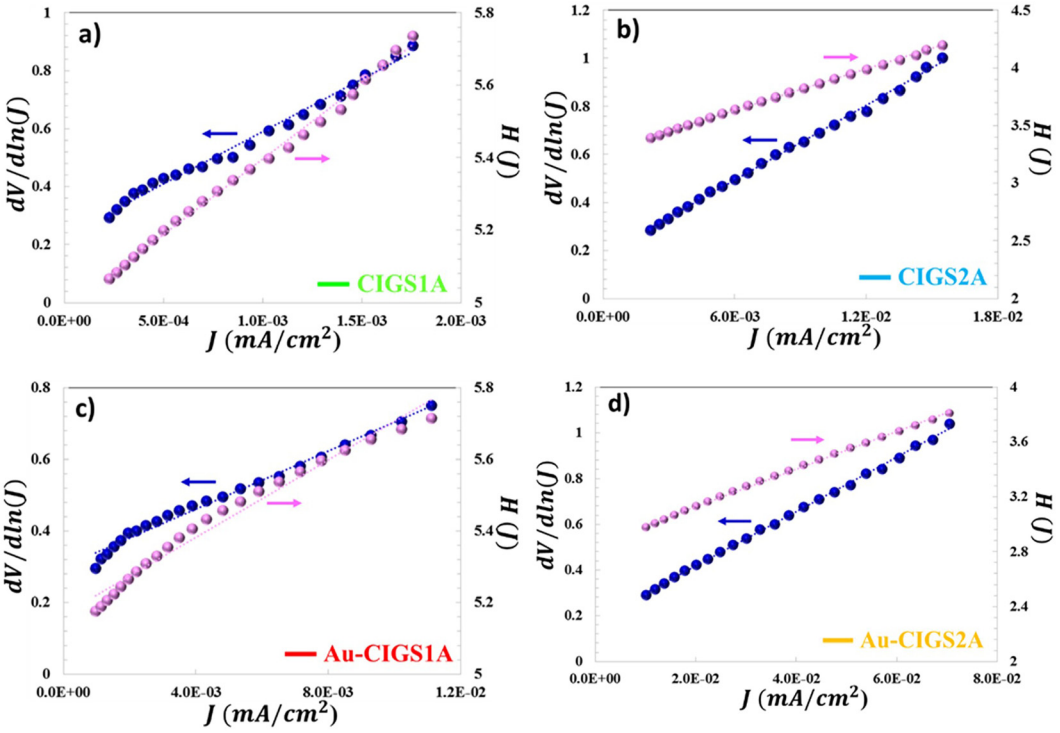

Figure 10: dV/dln (*J*)-*J* and H(*J*)-*J* curves of a) CIGS1A, b) CIGS2A, c) Au-CIGS1A and d) Au-CIGS2A hetero-junction structures in the darkness under a bias voltage range of +1.5 V, at room temperature.

Norde analyses are highly comparable, demonstrating a good correlation between the two methods. However, these parameters were evaluated using the conventional *J-V* technique are somewhat higher than those estimated through the Norde analysis, indicating minor discrepancies between the two methods.

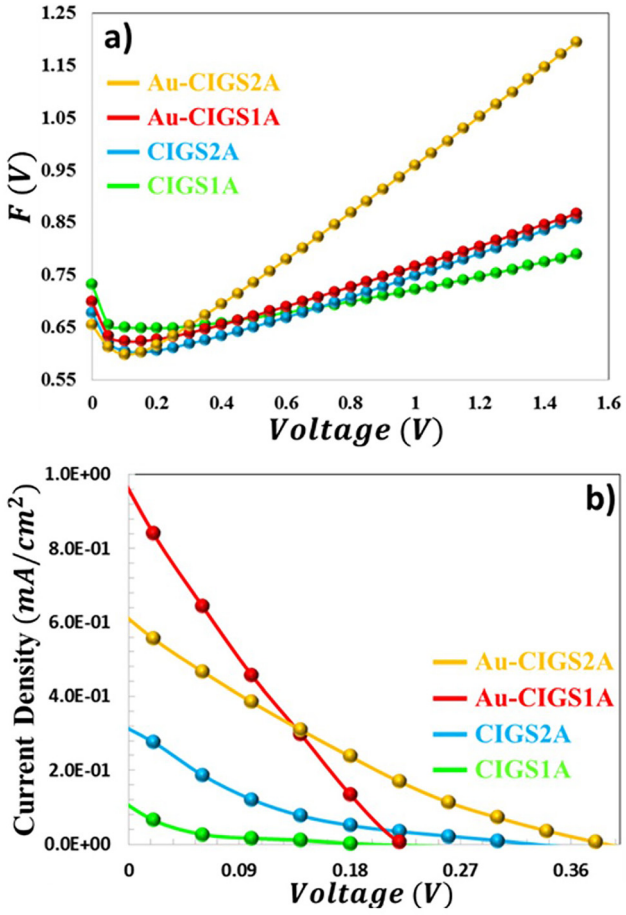

Figure 11: Photoresponse properties. (a) *F*(*V*)–*V* and (b) *J*-*V* characteristics of plasmonic and non-plasmonic CIGS/n-Si heterojunction structures measured in the dark, under a bias voltage range of +1.5 V, under AM 1.5 solar illumination (80 mW/cm^2), at room temperature, respectively.

3.5 Photovoltaic properties of plasmonic and non-plasmonic CIGS/n-Si heterojunction diodes

As seen from the J–V curves in Figure 11b and the data summarized in Table 4, all heterojunction diodes exhibit a photovoltaic response under AM 1.5 illumination with an incident power density of 80 mW/cm^2. The low photovoltaic efficiencies are mainly attributed to the reduced short-circuit current density (J_{sc}), which arises from insufficient optical absorption due to the ultrathin CIGS absorber layer. The limited absorption restricts the number of photo-generated charge carriers, thereby reducing the photocurrent density.

Increasing the absorber-layer thickness from CIGS1A to CIGS2A results in a noticeable improvement in photovoltaic performance. The refined crystalline structure and enlarged grain size extend the minority-carrier lifetime, suppressing the formation of defects and trap centers. CIGS1ultrathin layer, with a thickness of 75 nm, exhibits insufficient photon absorption capacity. Furthermore, the crystalline quality of the ultrathin CIGS1 film is notably suboptimal, suggesting numerous structural defects. These defects can act as recombination centers for minority charge carriers, thereby reducing their lifetimes. This reduction in carrier lifetime can increase series resistance, in turn decreasing Jsc. With increased thickness of ultrathin CIGS films (from 75 nm to 180 nm), their crystallinity improves, leading to a rise in average grain size. This structural enhancement mitigates the impact of defect sites, which previously acted as recombination centers for photo-excited charge carriers. As a result, the carrier lifetime is prolonged, thereby increasing Jsc. Moreover, as the diffusion length of the photo-generated charge carriers exceeds the film thickness, the carriers experience a longer lifetime. Consequently, the minority charge carriers can diffuse into the depletion region with minimal recombination, further enhancing device performance.

Au atoms can passivate surface states at the interface, leading to an extended carrier lifetime and, consequently, lower recombination rates. Furthermore, Au doping increases grain size and reduces the number of grain boundaries, thereby passivating defects and traps. In addition, Au can optimize local electric fields in CIGS, thereby improving electron transfer at the interface. This results in greater charge accumulation in the depletion region. As a result, the generation and collection of photocarriers are enhanced, while recombination losses are reduced, resulting in higher J_{sc} and V_{oc} values. The incorporation of Au plasmonic nanoparticles further improves the device performance. Compared with their non-plasmonic counterparts, the plasmonic Au-CIGS1A and Au-CIGS2A diodes exhibit higher J_{sc}, V_{oc}, and η, owing to a combination of LSPR-induced optical enhancement and improved structural quality of the CIGS layer. Additionally, reducing series resistance enhances photovoltaic efficiency by minimizing resistive losses and

Table 4: Photovoltaic parameters of plasmonic and non-plasmonic CIGS/n-Si heterojunction diodes under AM 1.5 solar illumination (80 mW/cm^2).

Sample	J_{sc} (mA/cm^2)	V_{oc} (mV)	FF (%)	η (%)
CIGS1A	0.15	180 mV	8.4	0.003
CIGS2A	0.31	340 mV	9.4	0.013
Au-CIGS1A	0.83	220 mV	25	0.044
Au-CIGS2A	0.66	380 mV	17	0.056

facilitating more efficient charge extraction across the junction.

The LSPR of plasmonic nanoparticles, together with near-field coupling between neighboring particles, leads to hot-electron generation and a pronounced enhancement of the photovoltaic parameters in CIGS/n-Si heterojunction diodes. Embedded Au nanoparticles in the CIGS layer support LSPR under illumination, generating hot electrons and enabling their transfer into the CIGS conduction band, thereby improving carrier dynamics and increasing device efficiency. As illustrated in the energy-band diagram (Figure 12), incident photons excite electrons in the Au nanoparticles from the Fermi level into the localized surface plasmon (LSP) mode; subsequent plasmon decay produces hot electrons that are injected into the conduction band of the CIGS semiconductor, thereby enhancing charge separation and carrier-injection efficiency.

Moreover, defect-level (DL) electrons in the CIGS layer can migrate toward the Au nanoparticles, where they gain additional kinetic energy through plasmonic interactions [60–63]. This process contributes to the passivation of defect states in the semiconductor and simultaneously enhances hot-electron generation and transport in the plasmonic–semiconductor structure [61, 62, 64–66]. Electrons with

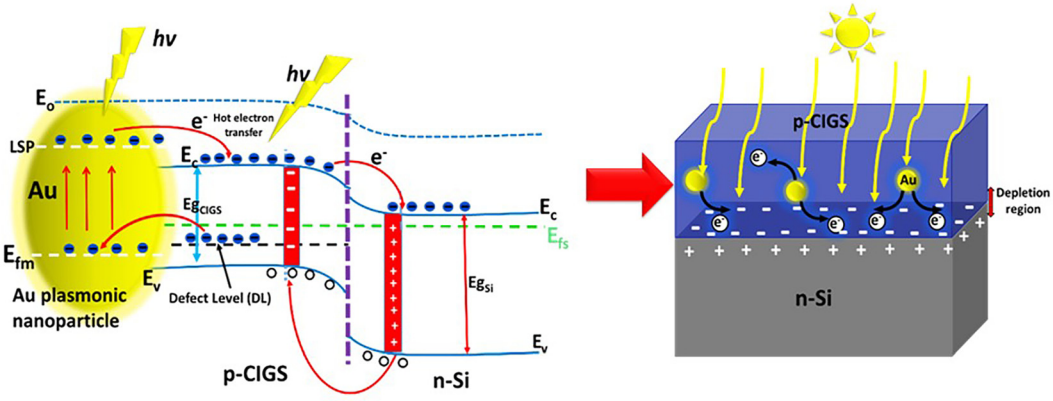

Figure 12: Schematic representation of the energy band alignment between the n-Si semiconductor and the Au nanoparticle–embedded CIGS absorber, illustrating LSPR-induced hot-electron generation in the Au nanoparticles and their injection across the CIGS/Si heterojunction interface.

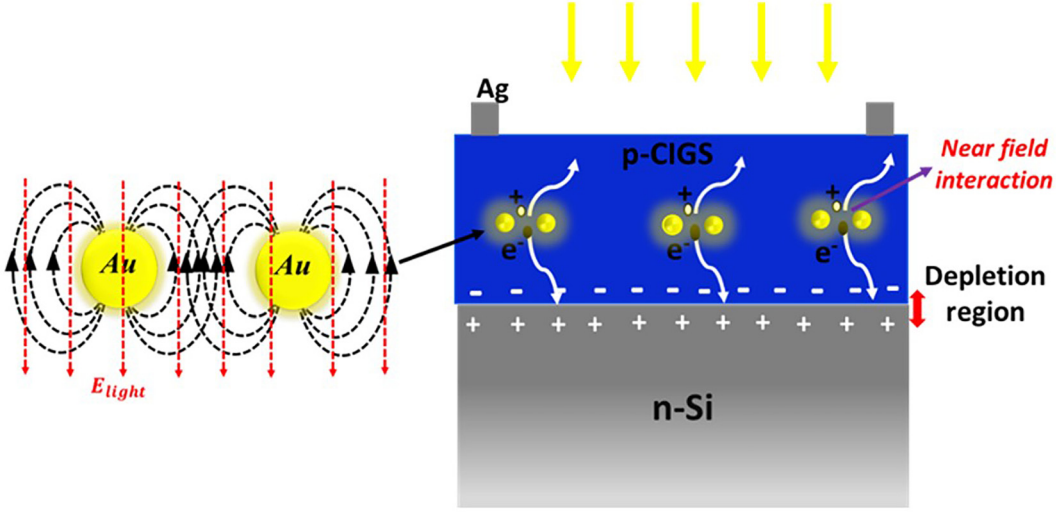

Figure 13: Schematic illustration of near-field enhancement arising from electromagnetic coupling between Au nanoparticles embedded in the CIGS ultrathin film and its effect on carrier generation in the *p*-CIGS/n-Si heterojunction.

elevated kinetic energy produced by LSPR excitation in the Au nanoparticles are efficiently transferred to the conduction band of the CIGS semiconductor, increasing the minority-carrier density in the vicinity of the depletion region [60, 63, 64, 67]. Provided their diffusion length is sufficient, these carriers can reach the junction edge and be effectively collected, thereby improving carrier extraction and overall device performance. Au nanoparticles can enable suitable band bending and an ideal built-in voltage between CIGS with different band gaps and Si semiconductors. Thus, rapid and efficient electron transfer from plasmonic CIGS semiconductors to Si is possible.

The near-field enhancement arises from electromagnetic coupling between adjacent Au nanoparticles embedded in the CIGS ultrathin films [65]. As evidenced by the spectral response in Figure 6, both Au-CIGS1 and Au-CIGS2 ultrathin films show increased photon absorption in the visible and near-infrared (NIR) regions due to the LSPR associated with the Au nanoparticles. So, when Au nanoparticles are positioned sufficiently close to one another in CIGS thin films, the electric field induced around an individual particle can be oriented opposite to the incident electromagnetic field generated by the incoming light, as illustrated in Figure 13. Under such conditions, strong near-field coupling arises between adjacent NPs due to electromagnetic interactions. This interparticle coupling perturbs the collective oscillatory motion of free electrons within the nanoparticles, thereby reducing the effective plasmon oscillation frequency. Consequently, LSPR peak undergoes a red shift toward longer wavelengths. Furthermore, the intensified electromagnetic field confined within the interparticle gap (so-called “hot spots”) results in significant local field enhancement. This enhanced near field promotes increased electron–hole pair generation in the surrounding semiconductor where the nanoparticles are embedded, thereby improving light–matter interaction in the system. This enhancement increases the number of photo-excited electron–hole pairs generated within these spectral ranges. In particular, the enhanced absorption in the visible region, which contributes most strongly to carrier generation, results in additional electron–hole pairs in the CIGS absorber layer. As a result, more minority carriers reach the depletion region with reduced recombination losses, thereby improving carrier collection efficiency and increasing the photocurrent density in the Au-CIGS1A and Au-CIGS2A heterojunction structures. Consequently, owing to the LSPR effect generated by the embedded Au plasmonic nanoparticles, the plasmon-enhanced CIGS/n-Si heterojunction diodes exhibit improved photovoltaic performance [17, 68–72]. In this study, Au nanoparticles are embedded into the mid-region of a CIGS thin film, and this is the first time plasmonic CIGS/n-Si heterojunction structures have been studied. Specifically, the placement of Au nanoparticles near the heterojunction interface (their presence at the interface could lead to defects) facilitates the transfer of photo-generated minority charge carriers and hot electrons into the depletion region, thereby increasing charge accumulation in this region. Furthermore, the ease with which the size and density of Au nanoparticles produced by the PLD system can be controlled, the ability to adjust the LSPR wavelength range, and the contribution of the LSPR effect to hot-electron generation are highly effective for photovoltaic performance. In addition, by developing the CIGS crystal structure with Au ions, the number of particle boundaries can be reduced, defects can be passivated, and charge transfer to the depletion region can be facilitated.

4 Conclusions

CIGS ultrathin absorbers with thicknesses of 75 nm and 180 nm were successfully grown by PLD and functionalized with Au plasmonic nanoparticles. Increasing the CIGS thickness and embedding Au led to pronounced grain growth, larger crystallites, reduced defect density, and a composition closer to the ideal Cu-poor CIGS stoichiometry, with evidence of partial Se–Au substitution. Independently grown Au nanoparticles exhibited tunable LSPR peaks, ranging from 564 to 772 nm, as the pulse number increased, confirming a controllable plasmonic response. These structural and compositional improvements resulted in stronger absorption in the UV–visible region, while the incorporation of Au added an LSPR-driven enhancement extending into the NIR. Electrically, the thinnest non-plasmonic device (CIGS1B) exhibited the highest ideality factor, series resistance, and barrier height, whereas the thicker, plasmonic Au-CIGS2B diode showed the lowest values and the best photovoltaic performance. Under AM 1.5 illumination (80 mW/cm^2), Au-CIGS2B delivered the highest J_{sc}, V_{oc}, fill factor, and efficiency, demonstrating that combining optimized CIGS thickness with Au nanoparticle–induced LSPR and hot-electron effects is an effective strategy for enhancing ultrathin CIGS/n-Si heterojunction solar cells.

Acknowledgments: The authors kindly wish to acknowledge Selçuk University High Technology Research and Application Center and Selçuk University Laser-Induced Proton Therapy Application and Research Center, for providing research infrastructure.
Funding information: Selçuk University Scientific Research Projects Coordination (BAP) Unit with project no. 21406007.

Author contributions: All authors have accepted responsibility for the entire content of this manuscript and approved its submission.

Conflict of interest: The authors state no conflict of interest.

Data availability statement: The datasets generated and/or analysed during the current study are available from the corresponding author on reasonable request.

References

1. Buecheler S, Pianezzi F, Reinhard P, Avancini E, Kranz L, Fu F, et al. C1GS thin film solar cells – breakthroughs for further efficiency improvements. Photovotaies at 2015;26:65–9.
2. Sivasankar SM, Amorim CDO, Cunha AFD. Progress in thin-film photovoltaics: a review of key strategies to enhance the efficiency of CIGS, CdTe, and CZTSSe solar cells. J Compos Sci 2025;9:143.
3. Yin G, Knight MW, van Lare MC, Solà Garcia MM, Polman A, Schmid M. Optoelectronic enhancement of ultrathin CuIn1–xGaxSe2 solar cells by nanophotonic contacts. Adv Opt Mater 2017;5:1600637.
4. Ali A, El-Mellouhi F, Mitra A, Aïssa B. Research progress of plasmonic nanostructure-enhanced photovoltaic solar cells. Nanomaterials 2022; 12:788.
5. Gezgin SY, Kepceoğlu A, Kılıç HŞ. An investigation of localised surface plasmon resonance (LSPR) of Ag nanoparticles produced by pulsed laser deposition (PLD) technique. In: AIP Conference Proceedings. Bodrum, Turkey: AIP Publishing LLC; 2016.
6. Linic S, Christopher P, Ingram DB. Plasmonic-metal nanostructures for efficient conversion of solar to chemical energy. Nat Mater 2011;10: 911–21.
7. Shan C, Huang Y, Wei J, Chen M, Wu L. Ultra-high thermally stable gold nanorods/radial mesoporous silica and their application in enhanced chemo-photothermal therapy. RSC Adv 2021;11:10416–24.
8. Masoud N, Partsch T, de Jong KP, de Jongh PE. Thermal stability of oxide-supported gold nanoparticles. Gold Bull 2019;52:105–14.
9. Gezgin SY, Kiliç HŞ. The effect of Ag plasmonic nanoparticles on the efficiency of CZTS solar cell: an experimental investigation and numerical modelling. Indian J Phys 2023;97:779–96.
10. García MA. Surface plasmons in metallic nanoparticles: fundamentals and applications. J Phys Appl Phys 2011;44:283001.
11. Noguez C. Surface plasmons on metal nanoparticles: the influence of shape and physical environment. J Phys Chem C 2007;111:3806–19.
12. Zarerasouli P, Bahador H, Heidarzadeh H. Performance improvement of an ultra-thin film solar cell based on optimized CIGS (Cu (In1-x, Gax) Se2) using appropriate plasmonic nanoparticles. Opt Mater 2022;131: 112729.
13. Londhe PU, Rohom AB, Chaure N. Improvement in the CIGS solar cell parameters by using plasmonic (Au) nanoparticle. Nanosci Nanotechnol 2016;6:43–6.
14. Zarerasouli P, Bahador H. Performance improvement of an ultra-thin film CIGS tandem solar cell using new plasmonic cluster nanostructures. Phys B Condens Matter 2024;687:416078.
15. Chen SC, Chen YJ, Chen WT, Yen YT, Kao TS, Chuang TY, et al. Toward omnidirectional light absorption by plasmonic effect for high-efficiency flexible nonvacuum Cu (In, Ga) Se2 thin film solar cells. ACS Nano 2014; 8:9341–8.
16. Zarerasouli P, Bahador H, Heidarzadeh H. Design of an efficient ultra-thin film Cu (In, Ga) Se2 solar cell, using plasmonic cluster back reflectors. Sol Energy 2023;261:1–6.
17. Park SU, Sharma R, Sim JK, Baek BJ, Ahn HK, Kim JS, et al. Development of gold induced surface plasmon enhanced CIGS absorption layer on polyimide substrate. Appl Surf Sci 2013;280:757–63.
18. Shepelin NA, Tehrani ZP, Ohannessian N, Schneider CW, Pergolesi D, Lippert T. A practical guide to pulsed laser deposition. Chem Soc Rev 2023;52:2294–321.
19. Gezgin SY, Belaid W, Kabatas MABM, Eker YR, Kilic HŞ. Microstrain effects of laser-ablated Au nanoparticles in enhancing CZTS-based 1 Sun photodetector devices. Phys Chem Chem Phys 2024;26:9534–45.
20. Oulmi N, Bouloufa A, Benhaya A, Mayouche R. CuIn 0.7 Ga 0.3 Se 2 thin films' properties grown by close-spaced vapor transport technique for second-generation solar cells. Mater Renew Sustain Energy 2019;8:1–8.
21. Chen SC, Hsieh DH, Jiang H, Liao YK, Lai FI, Chen CH, et al. Growth and characterization of Cu (In, Ga) Se 2 thin films by nanosecond and femtosecond pulsed laser deposition. Nanoscale Res Lett 2014;9:1–7.
22. Ghanbari E, Zahedifar M, Moradi M. Improving CIGS thin film by evaporation of CIGS nanoparticles without phase change. Appl Phys A 2019;125:1–9.
23. Gezgin SY. Modelling and investigation of the electrical properties of CIGS/n-Si heterojunction solar cells. Opt Mater 2022;131:112738.
24. Yao K, Li S, Liu Z, Ying Y, Dvořák P, Fei L, et al. Plasmon-induced trap filling at grain boundaries in perovskite solar cells. Light Sci Appl 2021; 10:219.
25. Yan X, Li J. Effect of film thickness of ZnO as the electron transport layer on the performance of organic photodetectors. Opt Mater 2022;128: 112438.
26. Zhang Y, Zhuang Y, Liu L, Qiu P, Su L, Teng X, et al. The microstructure evolution during MoS2 films growth and its influence on the MoS2 optical-electrical properties in MoS2/p-Si heterojunction solar cells. Superlattice Microst 2020;137:106352.
27. Yilmaz M, Kacus H, Grilli ML, Aydogan S. Effect of NiOx's film thickness on the electrical properties of Ni/p–NiOx/n-Si structures. J Sandw Struct Mater 2021;23:1383–402.
28. Gezgin SY, Houimi A, Kılıç HŞ. Production and photovoltaic characterisation of n-Si/p-CZTS heterojunction solar cells based on a CZTS ultrathin active layers. Optik 2019;199:163370.
29. Katerski A, Kärber E, Acik IO, Dolgov L, Mere A, Sildos I, et al. Modification of light absorption in thin CuInS2 films by sprayed Au nanoparticles. Nanoscale Res Lett 2014;9:494.
30. Qu S, Yuan X, Li Y, Li X, Zhou X, Xue X, et al. Aqueous synthesis of composition-tuned defects in CuInSe 2 nanocrystals for enhanced visible-light photocatalytic H 2 evolution. Nanoscale Adv 2021;3:2334–42.
31. Kristiawan B, Budiana EP, Abdulah A. Multi-technique characterization of TiO2 nanoparticles: crystallite size, microstrain, and phase analysis for nanomaterial applications–a review. Hybrid Adv 2025;11:100523.
32. Kalita PK, Sarma B, Das H. Structural characterization of vacuum evaporated ZnSe thin films. Bull Mater Sci 2000;23:313–17.
33. Prabahar S, Dhanam M. CdS thin films from two different chemical baths – structural and optical analysis. J Cryst Growth 2005;285:41–8.
34. Dolbec R, Irissou E, Chaker M, Guay D, Rosei F, El Khakani. Growth dynamics of pulsed laser deposited Pt nanoparticles on highly oriented pyrolitic graphite substrates. Phys Rev B Condens Matter 2004;70: 201406.
35. Kresz N, Smausz T, Hopp B. The dependence of the size distribution of the pulsed laser deposited micron sized particles from the laser fluence

and its influence to the thickness of the deposited layer. Appl Surf Sci 2007;253:8160–4.
36. Houck DW, Assaf EI, Shin H, Greene RM, Pernik DR, Korgel BA. Pervasive cation vacancies and antisite defects in copper indium diselenide (CuInSe2) nanocrystals. J Phys Chem C 2019;123:9544–51.
37. Siebentritt S, Igalson M, Persson C, Lany S. The electronic structure of chalcopyrites – bands, point defects and grain boundaries. Prog Photovoltaics Res Appl 2010;18:390–410.
38. Xu Y, Li Q. Heterostructured CIGS–Au nanoparticles: from Au–CIGS side-by-side structure to Au-core/CIGS-shell configuration. Nanoscale 2011;3:3238–43.
39. Zhang L, Zhuang D, Zhao M, Gong Q, Guo L, Ouyang L, et al. The effects of selenium content on Cu (InGa) Se2 thin film solar cells by sputtering from quaternary target with Se-free post annealing. Vacuum 2017;137: 205–8.
40. Lee H, Jang Y, Nam SW, Jung C, Choi PP, Gwak J, et al. Passivation of deep-level defects by cesium fluoride post-deposition treatment for improved device performance of Cu (In, Ga) Se2 solar cells. ACS Appl Mater Interfaces 2019;11:35653–60.
41. Martinsson E. Nanoplasmonic sensing using metal nanoparticles. Sweden: Linköping University Electronic Press; 2014.
42. Huang X, El-Sayed MA. Gold nanoparticles: optical properties and implementations in cancer diagnosis and photothermal therapy. J Adv Res 2010;1:13–28.
43. Cobley CM, Skrabalak SE, Campbell DJ, Xia Y. Shape-controlled synthesis of silver nanoparticles for plasmonic and sensing applications. Plasmonics 2009;4:171–9.
44. Atay T, Song J-H, Nurmikko AV. Strongly interacting plasmon nanoparticle pairs: from dipole− dipole interaction to conductively coupled regime. Nano Lett 2004;4:1627–31.
45. Zhu S, Chen TP, Cen ZH, Goh ESM, Yu SF, Liu YC, et al. Split of surface plasmon resonance of gold nanoparticles on silicon substrate: a study of dielectric functions. Opt Express 2010;18:21926–31.
46. Kişnişci Z, Özel FARUK, Yüksel ÖF, Tuğluoğlu N. Optical characterization of Cu2ZnSnS4 nanocrystals thin film. J Mater Sci Mater Electron 2016; 27:10128–35.
47. Royanian S, Abdolahzadeh Ziabari A, Yousefi R. Efficiency enhancement of ultra-thin CIGS solar cells using bandgap grading and embedding Au plasmonic nanoparticles. Plasmonics 2020;15:1173–82.
48. Chen SC, Wu KH, Li JX, Yabushita A, Tang SH, Luo CW, et al. In-situ probing plasmonic energy transfer in Cu (In, Ga) Se2 solar cells by ultrabroadband femtosecond pump-probe spectroscopy. Sci Rep 2015; 5:18354.
49. Kişnişci Z, Özel FARUK, Karadeniz S, Tuğluoğlu N, Özel SS, Yüksel ÖF. Electrical properties of Al/CZTSe nanocrystal Schottky diode. J Mater Sci Mater Electron 2024;35:773.
50. Tataroğlu ADEM, Aydın H, Al-Ghamdi AA, El-Tantawy F, Farooq WA, Yakuphanoglu F. Photoconducting properties of Cd 0.4 ZnO 0.6/p-Si photodiode by sol gel method. J Electroceram 2014;32: 369–75.
51. Ali SM, Ramay SM, Rehman NU, Ramzan K, Shar MA, Mahmood A. Fabrication and SILAR cycle-dependent characterization of CdS/p-Si heterojunction photodetector. J Mater Sci Mater Electron 2020;31: 2530–6.
52. Stanbery BJ, Abou-Ras D, Yamada A, Mansfield L. CIGS photovoltaics: reviewing an evolving paradigm. J Phys Appl Phys 2021;55:173001.
53. Gloeckler M, Sites JR, Metzger WK. Grain-boundary recombination in Cu (In, Ga) Se2 solar cells. J Appl Phys 2005;98:113704.
54. Machkih K, Oubaki R, Makha M. A review of CIGS thin film semiconductor deposition via sputtering and thermal evaporation for solar cell applications. Coatings 2024;14:1088.
55. Ashery A, Elnasharty MM, El Radaf I. Fabrication and electrical characterization of the Al/n-Si/CZTSe4/Ag heterojunction. Phys B Condens Matter 2021;609:412707.
56. Werner F, Veith-Wolf B, Melchiorre M, Babbe F, Schmidt J, Siebentritt S. Ultra-thin passivation layers in Cu (In, Ga) Se2 thin-film solar cells: full-area passivated front contacts and their impact on bulk doping. Sci Rep 2020;10:7530.
57. Muzzillo CP. Review of grain interior, grain boundary, and interface effects of K in CIGS solar cells: mechanisms for performance enhancement. Sol Energy Mater Sol Cell 2017;172:18–24.
58. Cheung S, Cheung N. Extraction of Schottky diode parameters from forward current-voltage characteristics. Appl Phys Lett 1986;49:85–7.
59. Norde H. A modified forward I-V plot for Schottky diodes with high series resistance. J Appl Phys 1979;50:5052–3.
60. Clavero C. Plasmon-induced hot-electron generation at nanoparticle/ metal-oxide interfaces for photovoltaic and photocatalytic devices. Nat Photonics 2014;8:95–103.
61. Khan R, Uthirakumar P, Bae KB, Leem SJ, Lee IH. Localized surface plasmon enhanced photoluminescence of ZnO nanosheets by Au nanoparticles. Mater Lett 2016;163:8–11.
62. Mousa AM, Ismail RA, Amin MH. Hybrid p-Au@ PbI2/n-Si heterojunction photodetector prepared by pulsed laser ablation in liquid. Optik 2019;183:933–41.
63. Valenti M, Jonsson MP, Biskos G, Schmidt-Ott A, Smith WA. Plasmonic nanoparticle-semiconductor composites for efficient solar water splitting. J Mater Chem A 2016;4:17891–912.
64. Meškinis Š, Peckus D, Vasiliauskas A, Čiegis A, Gudaitis R, Tamulevičius T, et al. Photovoltaic properties and ultrafast plasmon relaxation dynamics of diamond-like carbon nanocomposite films with embedded Ag nanoparticles. Nanoscale Res Lett 2017;12:1–10.
65. Wang L, Chen R, Ren ZF, Ge CW, Liu ZX, He SJ, et al. Plasmonic silver nanosphere enhanced ZnSe nanoribbon/Si heterojunction optoelectronic devices. Nanotechnology 2016;27:215202.
66. Boriskina SV, Ghasemi H, Chen G. Plasmonic materials for energy: from physics to applications. Mater Today 2013;16:375–86.
67. Ng C, Zeng P, Lloyd JA, Chakraborty D, Roberts A, Smith TA, et al. Plasmonic hot-carrier extraction: mechanisms of electron emission. arXiv preprint arXiv:1711.07095 2017.
68. Ananthoju B, Mopurisetty SM, Tyagi H, Bahadur D, Medhekar NV, Ganguly S, et al. Efficiency enhancement in Cu2ZnSnS4 solar cells with silica nanoparticles embedded in absorber layer. In: 2015 IEEE 42nd Photovoltaic Specialist Conference (PVSC). New Orleans, Louisiana, USA: IEEE; 2015.
69. Chen SC, Wu KH, Li JX, Yabushita A, Tang SH, Luo CW, et al. In-situ probing plasmonic energy transfer in Cu (In, Ga) Se 2 solar cells by ultrabroadband femtosecond pump-probe spectroscopy. Sci Rep 2015;5:18354.
70. Katerski A, Kärber E, Acik IO, Dolgov L, Mere A, Sildos I, et al. Modification of light absorption in thin CuInS 2 films by sprayed Au nanoparticles. Nanoscale Res Lett 2014;9:494.
71. Konda RB, Mundle R, Mustafa H, Bamiduro O, Pradhan AK, Roy UN, et al. Surface plasmon excitation via Au nanoparticles in n-Cd Se/ p-Si heterojunction diodes. Appl Phys Lett 2007;91:191111.
72. Zhang X, Wu X, Centeno A, Ryan MP, Alford NM, Riley DJ, et al. Significant broadband photocurrent enhancement by Au-CZTS core-shell nanostructured photocathodes. Sci Rep 2016;6:23364.